JOURNAL OF MATERIALS SCIENCE: MATERIALS IN MEDICINE 15 (2004) 237–247

Characterization of nanostructure phenomena in airborne particulate aggregates and their potential for respiratory health effects

L. E. MURR, E. V. ESQUIVEL, J. J. BANG
Department of Metallurgical and Materials Engineering, The University of Texas at El Paso, El Paso, TX 79968, USA

Airborne aggregates of nanoparticulates were collected on carbon/form-coated, 100-mesh Ni TEM grids in a thermal precipitator and observed in an analytical TEM utilizing a BF-SAED-DF-EDS characterization protocol to identify the nanocrystalline or nanoparticulate components, especially their degree of crystallinity, size, structural/morphologic features, and chemistries. Reference aggregates of TiO_2 rutile and anatase as well as Si_3N_4 nanoparticles were used to establish these characterization protocols, which were applied to several hundred individual particulates: homogeneous aggregates of carbonaceous/diesel particulate matter, complex mixtures of carbonaceous matter, including carbon nanocrystals, and inorganic nanocrystals; and heterogeneous, nanocrystal/nanoparticulate aggregates. Most airborne particulates were aggregates ranging in aerodynamic diameters from a few nanometers to a few microns; containing as few as 2 nanocrystals to several thousand nanocrystals or nanoparticulates such as carbonaceous spherules arranged in complex branched homogeneous aggregates composing diesel exhaust, with spherule diameters ranging from 10 to 30 nm. The potential for ultrafine airborne aggregates to fragment into hundreds or thousands of nanoparticulate components in human airways and act as toxic agents in deep lung tissue is demonstrated.

1. Introduction

Airborne particulate matter (PM) in the atmosphere is a complex mixture of suspended particles and particulate clusters and aggregates that vary in size, morphology, structure, and chemical composition. The sizes of ambient air particles range from roughly 0.005 μm (5 nm) to 100 μm in aerodynamic diameter. Urban airborne particulate size distributions normally exhibit three characteristic size regimes: ultrafine or nanoparticulates with aerodynamic diameters < 100 nm (designated $PM_{0.1}$), fine particulates with aerodynamic diameters < 2.5 μm ($PM_{2.5}$), and coarse regimes defined as particulates with aerodynamic diameters > 2.5 μm. Epidemiologic studies conducted over the last decade have shown that $> 90\%$ of mineral PM deposited in airway sites of human lungs had aerodynamic diameters < 2.5 μm ($PM_{2.5}$) [1]. Furthermore, ultrafine particulates were generally more detrimental to respiratory response than fine particulates, on a mass basis [2], and Momarca *et al*. [3] illustrated that fine crystalline silica PM had a more deleterious effect on lung epithelial cell damage than corresponding (fine) amorphous silica PM. In addition, recent airborne particulate analysis has shown that a very high fraction $(> 90\%)$ of fine and ultrafine particulates are aggregates and $> 80\%$ of these aggregates are crystalline or polycrystalline mixtures [4, 5]. The noncrystalline or semicrystalline fraction of particulates or particulate aggregates are largely carbonaceous PM, and many aggregates are complex mixtures of carbonaceous particles or a matrix of carbonaceous matter, even fullerene polyhedra, and inorganic crystalline or polycrystalline particles; usually of nanometer dimensions.

While ultrafine PM comprises only 1–8% of the total airborne PM mass [6], ultrafine particulates are present in large quantities, and in a fixed volume, have very large surface areas (or surface area to volume ratios) in contrast to the larger particulate regimes. In this regard, ultrafine particulates and particulate aggregates, especially nanocrystalline aggregates (and individual crystal polyhedra) would have a propensity for photocatalysis and thermocatalysis because of the regularity of the atomic structure [7]. However in the case of well-recognized photocatalysts such as TiO_2, the phase and structure are crucial for effective catalysis [8]. Correspondingly, Oberdörster *et al*. [9] found that intratracheal instillation of resuspended, ultrafine TiO_2 particles induced more of an inflammatory response than did fine TiO_2 particles.

In addition to the apparent respiratory health effects of particle size (ultrafine PM in particular) and crystallinity [3], there are also health effects associated with particle

composition [10–12], especially where components may detach or dissolve from particles and move into the bloodstream where they can reach other tissues outside the respiratory system [13, 14]. In some instances, particle toxicity may be a complex issue involving size, crystallinity and composition. Even particulate morphology may have a particularly unique effect, but morphology has not been studied, and in many studies involving particulate size regimes the particulates were not specifically observed nor their aerodynamic diameters individually measured. Consequently there are many uncertainties regarding the actual mechanism or mechanisms of particle effects, i.e. they may be morphologic, size-, structure-, composition (chemistry)-specific, or complex combinations of these phenomena.

The issue of particulate, or more specifically aggregate morphology, as well as aggregate structure and composition, may be very important in the context of respiratory health effects, especially particulate–tissue/cell interactions as these may relate to the mechanisms of toxicity. In particular, the ability of airborne aggregates to fragment during respiration, and upon reaching the alveoli space in the lungs, may be a significant attribute associated with particulate toxicity. Indeed, airborne aggregates range in size from two crystal grains to thousands of crystal grains or related individual components (such as amorphous, carbonaceous spherulites) which range in size from ~ 5 to 50 nm; with aggregate aerodynamic diameters as large as 2 μm [4, 15].

This study is concerned with the detailed characterization of a range of airborne particulate aggregates utilizing transmission electron microscopy (TEM) and ancillary techniques involving selected-area electron diffraction (SAED) and energy-dispersive (X-ray) spectrometry (EDS). The primary objective involved the examination and comparison of various aggregate and particulate morphologies as well as the characterization of the structure and composition of the nanoparticulates composing these aggregates. Here we will define aggregates as primarily heterogeneous agglomerates (particulates gathered into a whole airborne particle), or a group or assembly of primarily homogeneous nanoparticulates, including the same composition of nanoparticulates. Aggregates can be agglomerates of electrostatically charged particles, contiguous, bonded particles, or combinations thereof, i.e. mixtures of physisorption and chemisorption which characterize either physical contact or actual (chemical or structural) bonding, respectively.

2. Experimental details

Airborne particulates in this study were collected on 3 mm carbon/formvar-coated, 100-mesh nickel TEM grids mounted in a cold block (ice water cooled to $\sim 10\,^{\circ}$C) in a specially designed, portable thermal precipitator (TP) described in detail elsewhere [4, 5]. Sampling was performed in various outdoor locations in El Paso, TX, USA with the TP located 1.5 m above ground level. The experimental collection grids were placed in special encapsulating holders after 0.5 h or more collection periods. The thermal precipitator has been shown to provide efficient collection of very fine airborne PM [4, 5] and is more convenient to use than impact-type collectors. Collections are avoided in high-humidity environments because of water vapor condensation.

As a means to provide a baseline or control for particulate analysis, commercially produced nanoparticles of TiO_2-rutile (tetragonal: $a = 4.59$ Å; $c = 2.96$ Å) and TiO_2-anatase (tetragonal: $a = 3.79$ Å; $c = 9.51$ Å) were dispersed into calm, outdoor air ~ 1 m from the TP inlet (at a height of ~ 1.5 m) by placing a few grams in a petri dish, and wafting the particulates with a small, battery-operated fan; with the TP operated in the normal collection mode [4, 5] (0.5 h at 1.5 m above ground level). In addition, nanoparticulates of Si_3N_4 (amorphous) prepared by laser processing were also collected on the carbon/formvar-coated Ni TEM grids in the TP in a similar manner. These separate collections were examined, along with a wide range of other outdoor collections (including diesel truck stop areas and heavy traffic intersections).

The experimental grid samples were examined in a Hitachi H-8000 analytical TEM operated at 200 kV accelerating potential, and employing a goniometer-tilt stage. The TEM was also fitted with a light-element (Be) window, Noran 5500 EDS for elemental analysis. Systematic dark-field (DF) imaging was a key issue in the examination of particle aggregate microstructures utilizing specific SAED pattern reflection rings or spots. Particulate compositions and crystal structures were identified qualitatively utilizing EDS spectra and the measurement and identification of systematic d-spacings (interplanar spacings) from SAED patterns ($d = \lambda L/R$; where λL is the TEM camera constant and R is the ring or spot radii measured in the SAED pattern) and matching corresponding X-ray card file (JCPDS) data often identified specific chemistries and crystal structures [16]. The EDS spectrum was effectively calibrated or checked for a carbon signal from the carbon/formvar coating substrate which was roughly 50 nm thick by recording the spectrum with the beam on an aggregate and then shifting the aggregate out of the beam and recording the EDS spectrum for the nearby substrate.

3. Results

Figs. 1 and 2 illustrate comparisons of typical aggregates of commercially prepared nanopowders of TiO_2 rutile (Fig. 1) and TiO_2 anatase (Fig. 2) collected on carbon/formvar coated 100-mesh Ni TEM grids in the TP; and observed in the TEM. The corresponding EDS spectra (Fig. 1(d) and Fig. 2(d)) illustrate some silica (SiO_2) or silicate-contaminating nanoparticulates incorporated into the TiO_2 aggregates for both samples, probably by electrostatic attraction of the airborne nanosilicates to the TiO_2 aggregates. The hexagonal SiO_2 reflections are superimposed in the SAED pattern in the insert in Fig. 2(c). A copper silicate appears to be agglomerated with the TiO_2 nanoparticles in Fig. 1(a) as evident in the EDS spectrum of Fig. 1(d). Also note that no carbon background peak occurs in the EDS spectra. The lack of oxygen in the signal is often problematical and is probably due to discriminator levels or the aggregate position. The bright-field (BF) and aperture

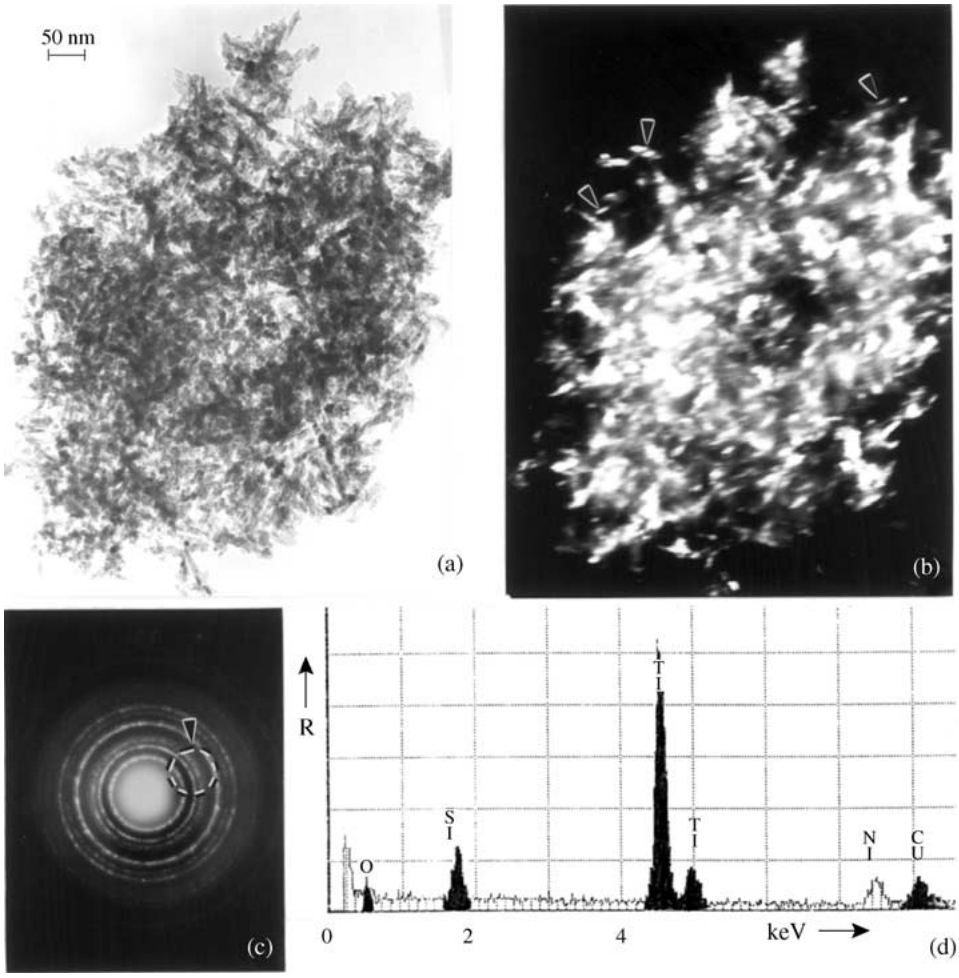

Figure 1 TiO_2 (rutile) reference sequence/protocol: (a) BF TEM image of TP collected aggregate, (b) DF image using aperture positioned as shown by dotted circle (arrow) in SAED patterns (c); corresponding to aggregate in (a). Arrows in (b) show individual nanocrystals. (d) EDS for aggregate in (a) showing Si and Cu contaminating peaks. Note Ni peak serves as a calibration. *R* denotes relative intensity in all EDS data to follow. Characteristic X-ray energies are in keV.

dark-field (DF) [16] sequences in Figs. 1 and 2 utilizing the corresponding SAED patterns and selected regions as shown by the dotted circle (and arrow) in the SAED pattern in Fig. 1(c) demonstrate the methodology for examining individual nanoparticulate components of airborne aggregates in this study. The DF images in Figs. 1(b), 2(b) and (c), respectively for rutile and anatase agglomerates show the distribution of the nanosilica and the primary nanocrystal components of the aggregated TiO_2 nanoparticulates. Nanocrystals ranging from 1 to 10 nm are shown by arrows in Fig. 1(b) and Fig. 2(c). The corresponding SAED pattern for TiO_2 anatase inserted in Fig. 2(c) shows generally finer nanocrystals in contrast to the more spotty rings in the SAED pattern for TiO_2 rutile in Fig. 1(c). The specific distribution of the SiO_2 nanocrystals is unknown. Note also the nanoparticulate component sizes and morphologies for the rutile and anatase polymorphs. These two examples (Figs. 1 and 2) serve as a baseline or reference for standardizing the analytical sequences to be illustrated in this study for particulate aggregates and clusters collected in the atmosphere using the TP.

The TiO_2 aggregates in Figs. 1 and 2 illustrate the propensity for airborne PM, especially aggregates, to attract or agglomerate with other airborne nanoparticulates, and in particular nanosilica particulates. This is particularly true for carbonaceous PM (especially carbon nanocrystal (fullerene) forms) which is often agglomerated with nanosilica or nanosilicate PM to form complex aggregates. Fig. 3 provides a number of very common examples of this feature in airborne PM. The analytical sequence represented in Fig. 3(a)–(c) also illustrates the ability of dense, complex aggregates to shed or particulate into individual nanofragments or nanocrystal particulates. The original aggregate in Fig. 3(a) was estimated to be 500 nm in diameter and when it contacted the carbon/formvar substrate in the TP collector it fragmented as shown. Individual or smaller PM components (carbon nanoforms) are shown by the arrows in Fig. 3(a) while the DF image in Fig. 3(b) utilizing the aperture position indicated in the SAED pattern insert in Fig. 3(a) illustrates the individual silica ($SiO_2 \cdot \alpha$-quartz; hexagonal: $a = 5.00$ Å, $c = 5.45$ Å) components to range from 2 to 25 nm in diameter. The estimated number of silica nanocrystals in the original aggregate (assuming an average nanocrystal diameter of 10 nm) was roughly 2000. This aggregate is effectively bound together with carbon nanocrystal forms similar to nanotubes or other fullerene-related nanocrystals as indicated in the SAED pattern insert in Fig. 3(a) and EDS spectrum in Fig. 3(c), and illustrated as a weak feature of the DF image in Fig. 3(b). It is especially

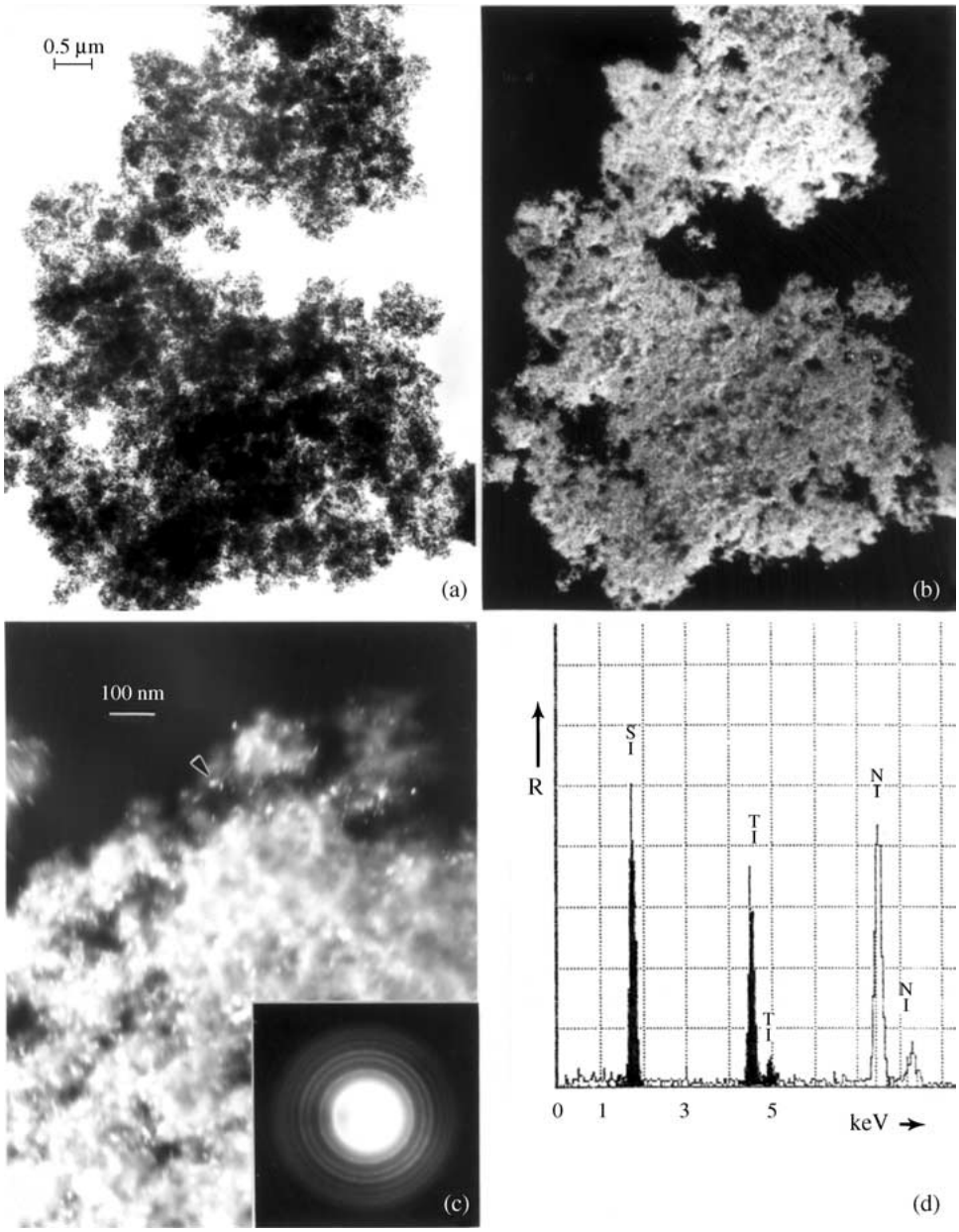

Figure 2 TiO_2 (anatase) reference. (a) BF image of large aggregate, (b) DF image of (a) utilizing the objective aperture positioned on the corresponding SAED pattern as in Fig. 1(c), (c) enlarged DF image with SAED pattern insert. Arrow shows individual nanocrystals, (d) EDS for aggregate in (a) showing large Si peak for agglomerated silica.

notable that the silica (101) reflection and the graphite (002) reflection coincide in forming the first SAED pattern reflection ring, corresponding to a *d*-spacing of 0.34 nm. In addition, the carbon peak in the EDS spectrum of Fig. 3(c) became essentially equivalent to the background noise when the beam was shifted off the aggregate onto the carbon/formvar coating. Fig. 3(d) and (e) shows this same silica-carbon nanocrystal feature for another complex aggregate having an SAED pattern and EDS spectrum similar to Fig. 3(a) and (c), respectively. The SiO_2 nanocrystals distributed in the DF image of Fig. 3(e) also range in size from roughly 2 to 25 nm as in Fig. 3(b), and the aggregate microstructure is also similar to Fig. 3(b). In Fig. 3(f) the BF–DF sequence shows larger SiO_2 nanocrystals (ranging from $\sim$ 10 to 125 nm) agglomerated with carbon nanocrystal forms or polyhedral material which appears as a nanocrystalline diffraction zone in the SAED pattern insert. The average aerodynamic diameter for the aggregate in Fig. 3(f) is approximately 1.2 µm and is the larger of the aggregates illustrated in Fig. 3.

Fig. 4 shows the agglomeration of presumably alumina (Al_2O_3) nanocrystals (ranging in size from 20 to 250 nm) around a larger particulate as shown especially prominent in the DF image of Fig. 4(c). While carbon does not appear in the EDS spectrum of Fig. 4(d), there is a faint, diffuse reflection indicated by the arrow in the SAED pattern of Fig. 4(b) which could be amorphous carbon.

Silicates, and especially larger silicate PM are very common in the atmosphere in many areas of the world especially in desert environments and many aerodynamic nanoparticulates can probably remain airborne for very long periods of time until agglomerated with other PM or altered somewhat by catalytic reactions of atmospheric gases and water vapor on their surfaces, forming more complex aggregates. Fig. 5 shows a small aggregation of overlapping, (layered talc nanoplates ($Mg_3(OH)_2Si_4O_{10}$: monoclinic; $a = 5.29$ Å, $b = 9.16$ Å, $c = 18.95$ Å). The

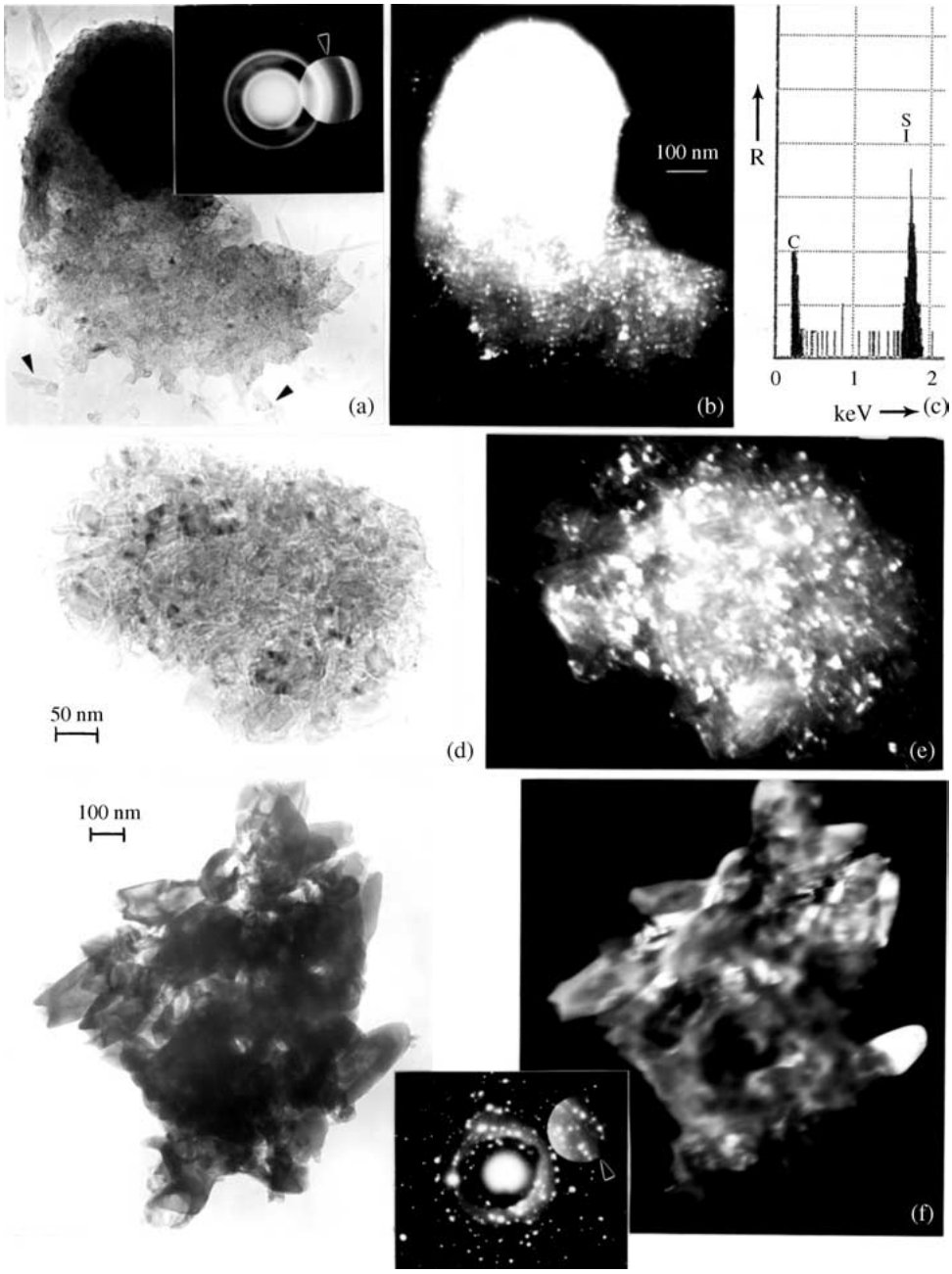

Figure 3 Examples of airborne nanocrystalline carbon–silica aggregates, (a)–(c) shows a BF–DF sequence utilizing the objective aperture positioned as shown in SAED insert (arrow) in (a) through a double exposure which enhances reflection rings, especially crystalline or nanocrystalline carbon, (d) EDS spectrum for (a) which is also typical for the other examples in (d) and (f). (d) and (e) show BF-DF sequence as in (a). (f) shows another BF–DF sequence for an aggregate containing larger nanocrystals. Note the difference between the SAED pattern inserts in (a) and (f). Note the magnification of (a) is the same as shown in (b).

SAED pattern (Fig. 5(b)) shows several systematically rotated crystal plates (note equivalent angles between prominent reflections) while the corresponding DF image in Fig. 5(c) shows dislocation structures and moire fringes in the crystal plates. Smaller, agglomerated aggregates of TiO_2 are shown by the arrows in Fig. 5(a), and the corresponding, weak, Ti peak is observed in the EDS spectrum in Fig. 5(d). The SAED pattern in Fig. 5(b) also contains superimposed rutile reflections. Certainly when ingested into the human airway the agglomerated TiO_2 nanoaggregates (Fig. 5(a)) could be expected to detach from the aggregate and attach to the epithelium. Note the crystal faceting/shape features evident in the upper nanoaggregate (arrow) in Fig. 5(a). Layered particulates such as talc and a variety of other silicates as well as graphitic PM may pose particularly unique features as a consequence of their ability to cleave into small crystal plates with a large, exposed surface area available for catalytic reactions involving other primary or secondary PM, water vapor and other gas-phase atmospheric components; and other, related heterogeneous nucleation phenomena.

For comparison with Figs. 1 and 2, Fig. 6 illustrates a typical, irregular, branched cluster particulate of commercially prepared (by laser processing of atomized nanoparticles) Si_3N_4 collected on a carbon/formvar-coated Ni TEM grid in the TP; and observed in the TEM. The corresponding SAED pattern for the cluster in Fig. 6(a) (in Fig. 3(b)) shows a characteristically amorphous (diffuse ring) structure (crystallite or pseudo-crystal sizes < 1 nm) except for a few crystalline zones indicated by a few spots in the pattern; and the DF

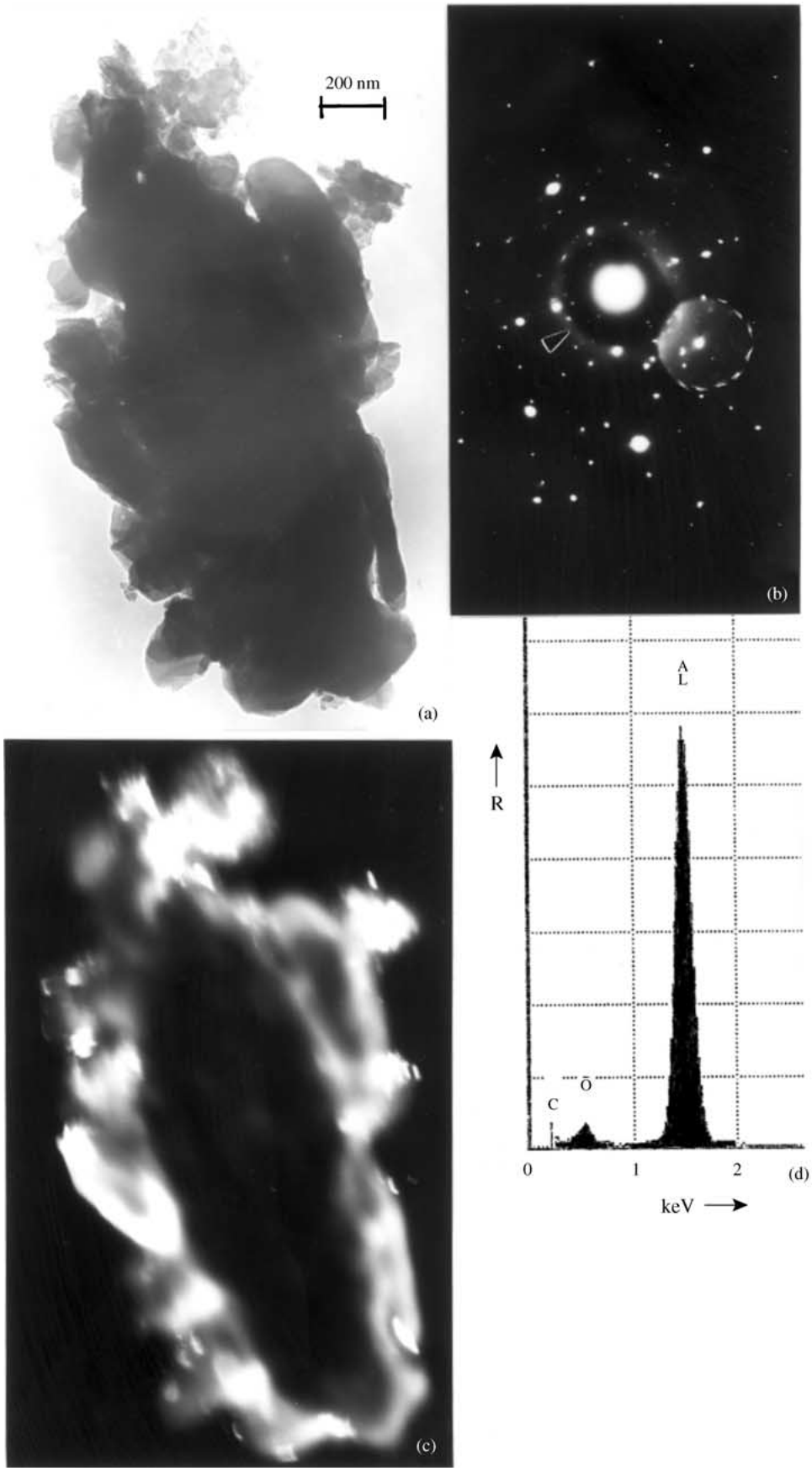

Figure 4 Agglomeration of larger Al_2O_3 nanocrystals around a core of PM of the same chemistry. (a) BF image, (b) SAED pattern for (a). Arrow indicates weak, diffuse reflection presumed to be carbon which does not appear in the EDS spectrum in (d). (c) shows the DF image of (a) using the objective aperture positioned as indicated by dotted circle in (b).

image in Fig. 6(c) shows a generally homogeneous, sub-nanocrystalline/amorphous structure. The nitrogen X-ray signal is absent in the EDS pattern of Fig. 6(e) and because the SAED pattern does not contain any crystal diffraction the composition is ambiguous. The morphologies of the individual (primary) nanoparticulates composing the cluster branches are generally spherules and similar in appearance to the carbonaceous spherules

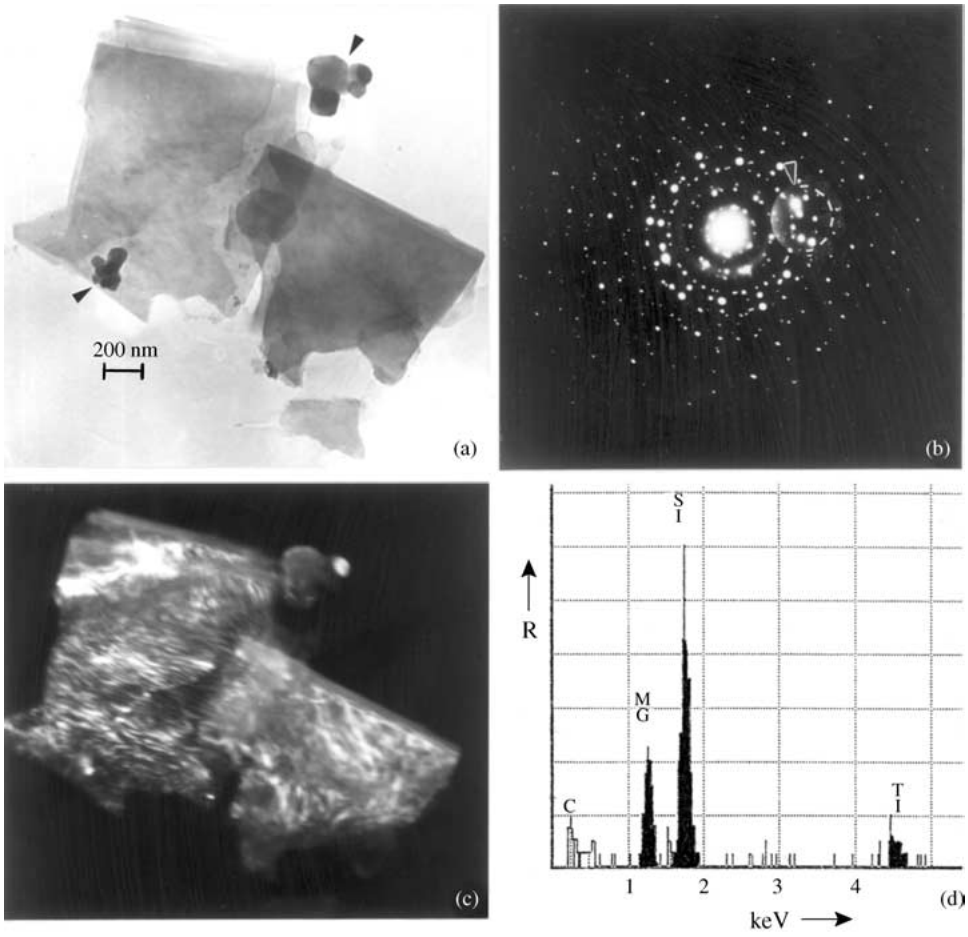

Figure 5 Layer silicate (talc) PM with agglomerated aggregates of TiO_2 nanocrystals. (a) BF image. Arrows show TiO_2 aggregates, (b) SAED pattern for (a). (c) DF image utilizing reflections circled and indicated by arrows in (b). (d) EDS spectrum for (a). Oxygen peak is absent.

characteristic of the irregular, branched clusters of amorphous, carbonaceous or hydrocarbon spherules observed for diesel particulate matter (DPM) [17]. The average cluster diameter in Fig. 6(a) is roughly 1.4 μm and is composed of approximately 1700 spherules. The slightly enlarged view in Fig. 6(d) shows for comparison with Figs. 1(a) and 2(a) some differences in crystalline, primary nanoparticulate component morphologies in contrast to amorphous component morphologies. The individual spherule sizes in the cluster of Fig. 6(d) range from roughly 5 to 30 nm. Figs. 1–3 also illustrate the aggregation and clustering phenomena which is typical of airborne PM [4, 5, 17].

Fig. 7 shows for comparison with Fig. 6 the typical structural and morphological features of airborne DPM to be characterized by the same irregular, branched, aggregate morphology composed of individual, primary spherules. The formation of these agglomerates (Fig. 7(a), (d) and (f) are, as noted in comparison with Fig. 6, generally unaffected by chemical composition [18] and they form by either strong forces involving ballistic impact and partial coalescence or by diffusion-limited aggregation [18, 19]. The variation in the overall aggregate size and the fractal geometries of the nano-spherules illustrated on comparing Fig. 7(a) with Fig. 8(d) and (f) is characteristic of variations in DPM which occur with variations in combustion temperatures, combustion efficiencies, and fuels or fuel-to-air ratios. The irregular, branched DPM aggregate morphologies have often been described and compared by various fractal dimensions [17, 20], e.g.; $N_p = A(R_a/R')D_f$; where N_p is the number of primary particles in the cluster, A is a constant, R_a is the characteristic radius of the cluster or radius of gyration, R' is the average primary particle radius, and D_f is the fractal dimension which apparently ranges from roughly 1 to 2 [17, 20]. Katrinak *et al*. [17] found that DPM in the Phoenix, AZ air was composed of 32–1842 spherules; with an average of 550 primary spherule particles in an aggregate. The spherule diameters ranged from 10 to 40 nm, [17]. In contrast, the number of spherules in Fig. 7(a) was roughly 700 with spherule diameters ranging from 10 to 30 nm while the number of spherules in the larger, more fractal-like (branched) aggregates of Fig. 7(d) and (f) varied between 250 and 350, with diameters similar to those in the larger aggregate in Fig. 7(a). The average particle or aggregate size or length in Fig. 7 varies from roughly 0.55 to 0.8 μm which is consistent with sizes of 0.2–2.6 μm for DPM in the Phoenix aerosol [17].

It is apparent on examining the irregular, branched aggregates in Fig. 7(d) and (e) in particular that these branches would be expected to be easily broken and redispersed in the lung tissue because of their extensive fragile branch structure. In fact, the aggregate features of DPM actually deposited in the alveolar epithelium would be expected to play a significant role in the efficiency of phagocytosis by macrophages as well as the release of polycyclic aromatic hydrocarbons (PAHs), or the catalytic production of other toxic agents contributing to cell mutations leading to carcinogenisis [21]. PAHs are

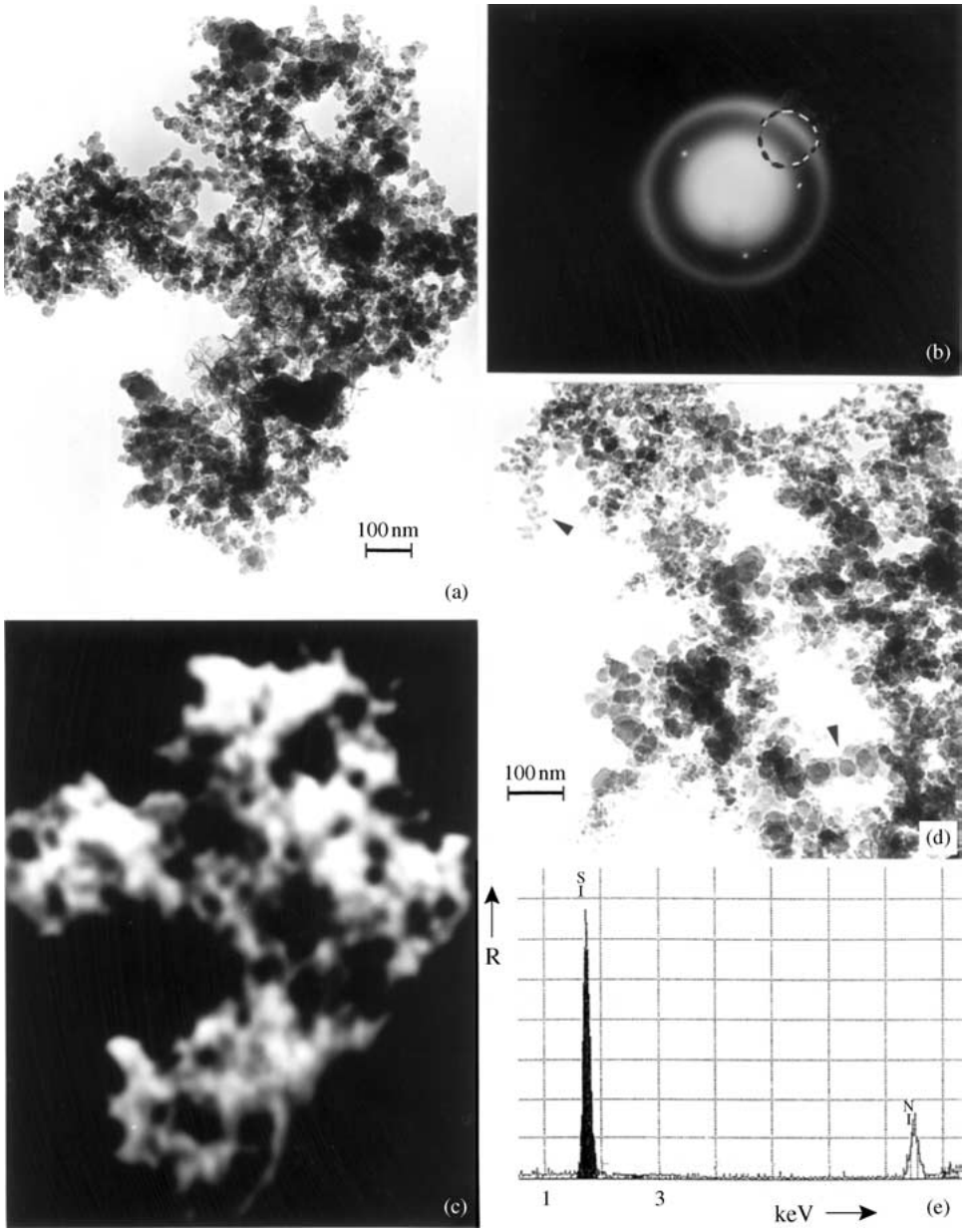

Figure 6 Si_3N_4 reference sequence. (a) BF image of cluster, (b) SAED pattern for (a). (c) DF image of (a) utilizing objective aperture positioned as shown by dotted circle in (b). (d) enlarged BF image showing complex, branching of small and large spherules. (e) EDS spectrum for (a). Nitrogen signal does not appear in the spectrum.

produced abundantly in any incomplete combustion of organic material. The notion that very large PM aggregates can degenerate into much smaller fragments or even hundreds or thousands of individual nanoparticulates is illustrated by the fragmentation, degradation, or shedding of nanocomponents in the vicinity of and by a particulate deposited on the carbon/formvar coating on a Ni TEM grid in the TP in Fig. 3(a) and (b). It is also evident on comparing the SAED pattern insert in Fig. 3(a) with that shown in Fig. 7(b) that very diffuse reflections occur for the aggregated carbonaceous spherules in contrast to the carbon nanocrystals composing the aggregate in Fig. 3(a).

As noted for the EDS data corresponding to Fig. 7(d) and (e) but not shown, trace amounts of Cu occur, and the DF image of Fig. 7(e) may be indicative that elements like Cu are not homogeneously distributed within the spherules. DPM and other species of PM containing trace elements such as Si, Ti, Fe, Cu, Zn, and Cr among others can catalyze the production of oxygen-free radicals such as superoxide (O_2^-) and hydroxyl radical (OH) by auto oxidation of quinone and polyphenol compounds. Consequently, oxygen-free radicals generated by DPM may cause mutations in the lung; and in fact oxidative damage to DNA was shown to increase in mouse lung during tumorigenesis by DPM [21, 22].

Finally, Fig. 8 illustrates the occurrence of other, more complex aggregates in a diesel smoke environment since it was collected on the same TP-TEM grid as the DPM cluster shown in Fig. 7(a)–(c). In Fig. 8, somewhat consistent with other examples of complex, airborne aggregates/agglomerates in Figs. 3–5, an array of different nanocrystalline PM is bound in a matrix of carbonaceous matter (diffuse reflection shown at arrow in Fig. 8(b)) as illustrated in the SAED pattern in Fig. 8(b), and the corresponding EDS data in Fig. 8(d). The multiple diffraction effects shown in the SAED pattern of Fig. 8(b) make specific nanocrystalline component identities difficult to determine, although elemental Ag (fcc) (prominent peak in the EDS spectrum of Fig. 8(d))

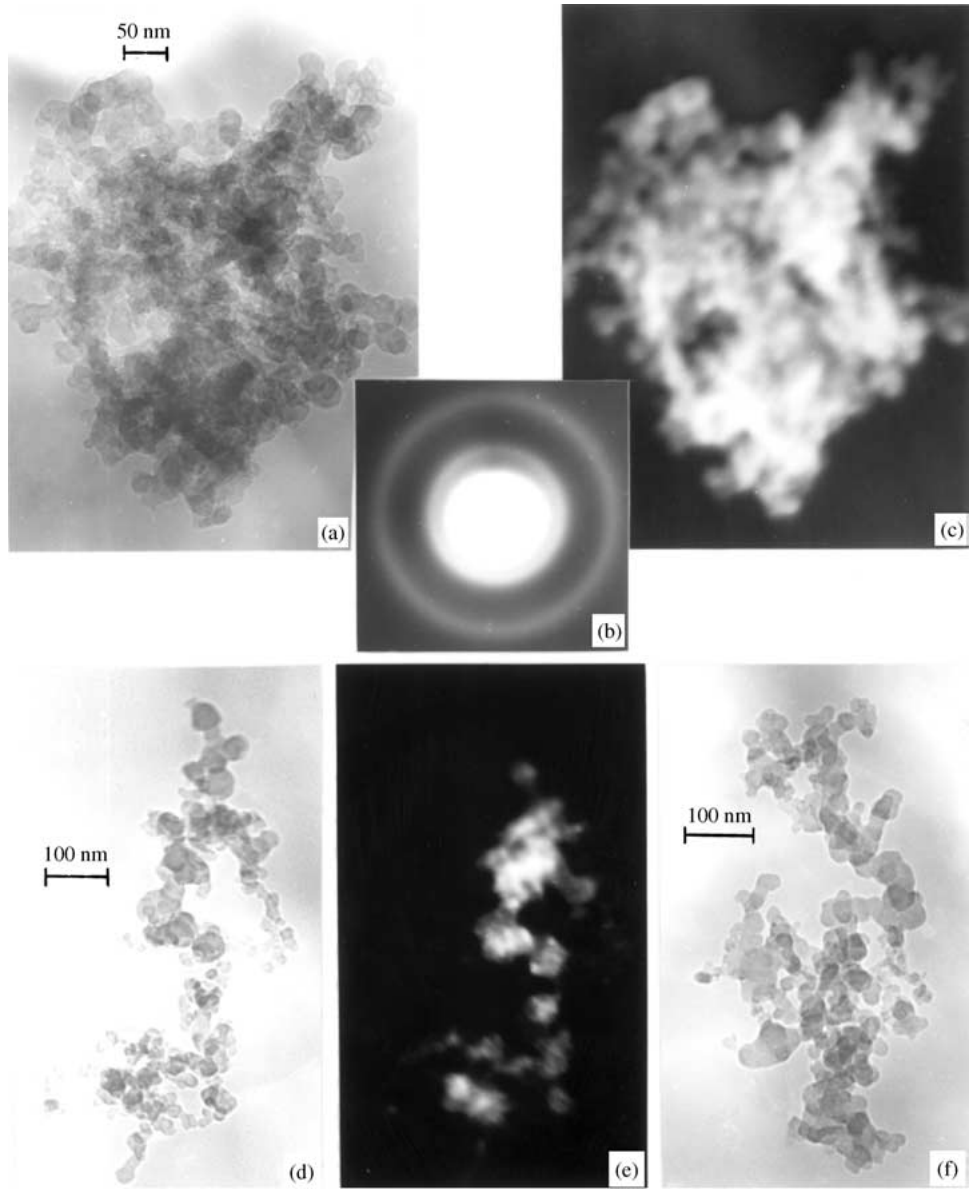

Figure 7 DPM clusters, (a) BF image of cluster collected in diesel truck stop area, (b) SAED diffuse ring pattern typical for (a), (d), and (f). (c) DF image of (a). (d) and (e) show BF–DF sequence for smaller cluster collected for small diesel engine exhaust. (f) shows a BF image for another DPM cluster.

and charcopyrite ($CuFeS_2$ – tetragonal) are possible. It is interesting to note that all of the aggregated PM species fall within the same size range (Fig. 8(c)): ≤ 5 nm–~ 40 nm aerodynamic diameter.

4. Discussion

Of more than 250 particulates collected and characterized in this and related investigations [4, 5], nearly 90% were aggregates or clusters and 85% were crystalline. Approximately 30% of the aggregates were either carbonaceous or contained carbonaceous matter which was essentially amorphous or semicrystalline.

In retrospect, it is interesting to note that while a very large fraction of airborne PM occurs as aggregates which can range in size from a few particles to a few thousand particles, a very significant proportion of these aggregates (excluding the characteristically aggregated, branched DPM) involve carbonaceous material which often acts like a binder or matrix. It is interesting to note that this aggregation of carbonaceous matter with other airborne PM may be a natural phenomenon or certainly a historical issue because TEM analysis of the lung tissue for the 5300-year old Tyrolean iceman [23] showed numerous anthracotic areas where carbonaceous matter was mixed with silica or silicates, characteristic of the observations of carbonaceous-silica aggregates in the airborne particulate samplings illustrated in Fig. 3 in particular. In fact, even TiO_2 nanocrystals were observed in the iceman's lungs, indicative of the fact that airborne TiO_2 particulates were in the atmosphere in antiquity. Of course the implications of these observations are not entirely clear, but certainly we cannot assume that complex aggregates containing nanocrystalline particulates which make up the bulk of contemporary air are necessarily the result of industrialization or of recent technological origin.

Current ambient air quality standards in the United States as well as contemporary efforts to revise them are based largely on epidemiological data that show an association between adverse health effects and especially ultrafine PM as noted earlier. More scientifically

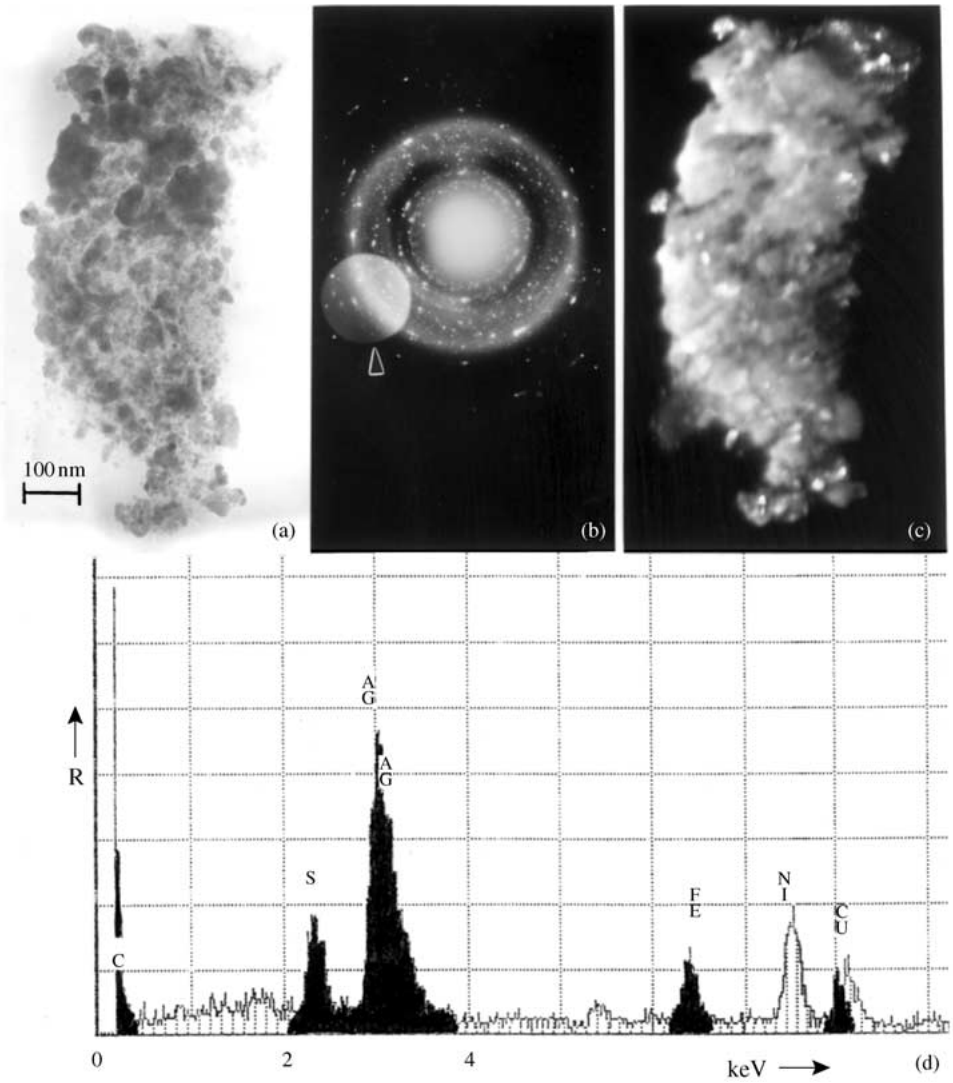

Figure 8 Complex aggregate collected on the same TP substrate as Fig. 7(a). (a) BF image, (b) SAED pattern for (a) showing double exposure of objective aperture (arrow), (c) DF image of (a) using objective aperture positioned as shown (arrow) in SAED pattern of (b). (d) EDS spectrum for (a). Ag peak is most prominent signal component.

defensible standards can only be established by the identification of specific chemical and/or physical agents attributable to respiratory health effects. In addition, the specific effects of ultrafine and nanoparticulates in the alveolar epithelium must also be understood if preventive or corrective measures are to be taken. This research has demonstrated that individual airborne PM within specific or characteristic size regimes is further complicated by aggregation and clustering phenomena which constitutes a very significant proportion ($\sim 85\%$) of all fine and ultrafine airborne PM, while nearly this same proportion of the ambient airborne PM is crystalline, or contains variously distributed collections of nanocrystalline components or primary nanoparticulates [4, 5]. Since ultrafine PM has been demonstrated to be particularly toxic [2] and especially prevalent in deep lung tissue [1], it is highly likely that nanoparticulate fragments from larger aggregates (1–2 μm mean aerodynamic diameter) as illustrated in this work may pose an even greater threat to respiratory health. In addition, since nanoparticle fragments are largely crystalline, they can also act as effective catalysts [7] in promoting additional, secondary reaction products which would also be transported to the alveolar epithelium. Indeed, because the specifics of nanoparticulate toxicity are not known, the effects could be particle size and morphology or crystal structure related, chemical species effects, or a combination. More detailed clinical studies involving specific aggregates and clusters and their observation in the respiratory tract as well as deep lung tissue may provide a more detailed resolution of these issues utilizing the characterization protocols illustrated herein.

5. Summary and conclusions

A higher fraction of airborne PM is aggregated, with aggregates composed of several to more than 2000 particles. A significant proportion of the airborne aggregates contain amorphous or semicrystalline, carbonaceous matter which often acts like a binder or matrix for other aggregated nanocrystalline particles. These particles or primary PM components range in size from roughly 5 to 50 nm for the most part. In addition, DPM includes aggregates of carbonaceous spherules forming complex and even fractal-like structures where inorganic nanocrystals are also often incorporated into the carbonaceous spherules. Consequently, most airborne aggregate PM, and therefore most airborne PM, contains

nanocrystal components. DPM aggregates can be as large as several microns on a side, and consist of several hundred to several thousand carbonaceous spherules ranging in size from 10 to 30 nm. These branched DPM aggregates as well as other large, complex airborne aggregates can easily fragment into much smaller components and even down to primary particulates in the human airways to produce hundreds or even thousands of nanocrystals which may be particularly toxic in the human respiratory tract.

Utilizing the characterization protocols involving TP collection and TEM analysis of airborne PM illustrated in this research can allow for more systematic and detailed analysis especially of ultrafine and nanoparticulates and their sources, as well as their disposition in deep lung tissue, including macrophage phagocytosis issues. Combustion efficiencies have already been demonstrated to alter the characteristics of DPM clusters and cluster structures and efficient pyrolysis in other commercial systems may also promote the production of larger and less fragile airborne, aggregate PM. It is becoming apparent that the elimination of nano-PM or aggregation of primary nano-PM by forming much larger, robust particulates may be an appropriate control mechanism to eliminate the escalation of respiratory illnesses worldwide.

Acknowledgments

This research was supported in part by an EPA-Southwest Center for Environmental Research and Policy (SCERP) Grant (Project A-02-5) and by a Mr and Mrs MacIntosh Murchison Endowment at the University of Texas at El Paso.

References

1. R. CHURG, M. BAURE, S. VERDAL and B. STEVENS, *J. Environ. Med.* **1** (1999) 39.
2. L. C. RENWICK, K. DONALDSON and A. CLOUTER, *Toxical. Appl. Pharmacol.* **172** (2001) 119.
3. S. MOMARCA, R. CREBELLI, D. TERRETTI, A. ZANARDINI, S. FUSELLI and L. FILINI, *Sci. Total Environ.* **205** (1997) 137.
4. J. J. BANG and L. E. MURR, *JOM*, **54** (2002) 28.
5. J. J. BANG, E. A. TRILLO and L. E. MURR, *J. Air Waste Managmt. Assoc.* **53** (2003) 227.
6. Environmental Protection Agency (US), ''Air Quality Criteria for Particulate Matter'', vol. III, EPA/600/P-95/001CF (National Center for Environ. Assessment, Research Triangle Park, NC, 1996).
7. R. R. CHIANELLI, M. J. YACAMAN, J. ARENAS and F. ALDAPE, *J. Hazardous Substance Res.* **1** (1998) 1.
8. M. R. HOFFMANN, *Chem. Rev.* **95** (1995) 69.
9. G. OBERDÖRSTER, J. N. FINKELSTEIN, C. JOHNSTON, R. GELEIN, C. COX, R. BAGGS and A. C. P. ELDER, *Res. Report* **96** ''Acute Pulmonary Effects of Ultrafine Particles in Rats and Mice'', (Health Effects Institute, Cambridge, MA, 2000).
10. R. T. BURNETT, J. BROOK, T. DANN, C. DELOCLA, D. PHILIPS, S. CAKMAK, R. VINCENT, M. S. GOLDBERG and D. KREWSKI, *Inhal. Toxicol.* **12**(Suppl. 4) (2000) 15.
11. W. P. WATKINSON, M. J. CAMPEN and D. L. COSTA, *Toxicol. Sci.* **41** (1998) 209.
12. R. W. CLARKE, B. GOULL, U. REINICH, P. CATALANO, C. R. KILLINGSWORTH, P. KOUTRAKIS, I. KAVOURAS, G. GAZULA, K. MURTHY, J. LAWRENCE, E. LOVETT, J. M. WOLFSON, R. L. VERRIER and J. J. GODLESKI, *Environ. Health Perspect.* **108** (2000) 1179.
13. A. NEMMAR, P. H. M. HOET, B. VAN QUICKENBORNE, D. DINSDALE, M. THOMEER, M. F. HOYLAERTS, H. VAN BILLOEN, L. MORTELMANS and B. NEMERY, *Circulation* **105** (2002) 411.
14. A. NEMMAR, H. VAN BILLOEN, M. F. HOYLAERTS, P. H. M. HOET, A. VERBRUGGEN and B. NEMERY, *Amer. J. Respir. Crit Care Med.* **164** (2001) 1665.
15. J. J. BANG and L. E. MURR, *J. Mater. Sci. Lett.*, **21** (2002) 361.
16. L. E. MURR, ''Electron and Ion Microscopy and Microanalysis: Principles and Applications'', 2nd edn (Marcel Dekker, New York, 1991).
17. K. W. KATRINAK, P. REZ, P. R. PERKES and P. R. BUSECK, *Environ. Sci. Tech.* **27** (1993) 639.
18. P. MEAKIN, *Phys. Rev. Lett.* **51** (1983) 1119.
19. T. A. WHITTEN and L. M. SANDER, *Phys. Rev. B* **27** (1983) 5686.
20. G. SKILLAS, S. KUNZEL, H. BURTSCHER, U. BALTENSPERGER and K. SIEGMAN, *J. Aerosol. Sci.* **29** (1998) 411.
21. H. SATO, H. SONE, M. SAGAI, K. T. SUZUKI and Y. AOKI, *Carcinogenisis*, **21** (2000) 653.
22. A. E. NEL, D. DIAZ-SANCHEZ and N. LI, *Curr. Opin. Pulm. Med.* **7** (2001) 201.
23. F. HOFER, C. MITTERBAUER, I. PAPST and M. A. PABST, *Eurem* **12** (2002) B413.

Received 4 April
and accepted 10 September 2003